

## Bandwidth oriented approach for the design of a PI controller for a three phase two-stage grid-connected PV system

Anshu Prakash Murdan, Iqbal Jahmeerbacus & S Z Sayed Hassen

**To cite this article:** Anshu Prakash Murdan, Iqbal Jahmeerbacus & S Z Sayed Hassen (2023): Bandwidth oriented approach for the design of a PI controller for a three phase two-stage grid-connected PV system, International Journal of Electronics, DOI: [10.1080/00207217.2023.2210299](https://doi.org/10.1080/00207217.2023.2210299)

**To link to this article:** <https://doi.org/10.1080/00207217.2023.2210299>



Published online: 16 May 2023.



Submit your article to this journal



Article views: 7



View related articles



View Crossmark data



# Bandwidth oriented approach for the design of a PI controller for a three phase two-stage grid-connected PV system

Anshu Prakash Murdan , Iqbal Jahmeerbacus and S Z Sayed Hassen

Department of Electrical and Electronic Engineering, University of Mauritius, Reduit, Mauritius

## ABSTRACT

The two-stage power converter is currently the most widespread topology for three-phase grid-connected photovoltaic (PV) systems. The PV power is injected to the grid through the regulation of the dc-link voltage. This method is commonly called the voltage control method, whereby the current is controlled indirectly. This paper focuses on the modelling of power converters and the parameter design of proportional-integral (PI) controllers, based on the bandwidth of the inner current loop and the outer voltage loop. It is assumed that the inner loop has a bandwidth that is ten-fold bigger than that of the outer loop, in order to fully decouple the dual loops. The PI parameters are thus determined through this relationship, and two sets of simulations are run to validate the methodology used. Results show that the controllers give highly satisfactory performance even in the presence of transients introduced by rapidly varying irradiance model.

## ARTICLE HISTORY

Received 1 July 2022

Accepted 9 April 2023

## KEYWORDS

Current loop; voltage loop;  
Park and Clark  
transformations; pulse-width  
modulation; voltage  
regulation

## 1. Introduction

The last decade has witnessed an upsurge in the adoption of solar photovoltaic (PV) systems for the production of green and clean energy. Along with wind energy systems, solar PV is one of the fastest-growing, mature and cost-competitive renewable energy technologies (IRENA, 2019). A PV array produces dc power which is converted into ac power by the power conditioning unit (PCU). The conversion is done according to grid requirements regarding voltage and power quality. However, for maximum power transfer to a load or to the grid, the power converters play an important role. The PCU may comprise a single-stage dc-ac converter or a two-stage converter (Xiao et al., 2013), with a dc-dc converter followed by dc-ac converter, commonly known as the inverter. The two-stage converter is more often used due to comparatively lesser number of PV panels involved, as well as better control (Debnath & Chatterjee, 2015; Kanaan et al., 2014). A maximum power point tracking (MPPT) algorithm is typically used for extracting maximum available power from PV modules (Manna et al., 2023). The maximisation of PV power is handled by the dc-dc converter stage, while the synchronisation with the ac grid is taken care of by the dc-ac inverter stage. Several MPPT techniques have been proposed by researchers, and a vast amount of work has been done to enhance these

techniques (Abdulhasan Salim et al., 2022; Bollipo et al., 2021; Hassan et al., 2023; Oshaba et al., 2017a, 2017b). Enhancements aim to provide better tracking under a wide range of environmental conditions, for example, fast varying solar irradiance, PV shading and partially shaded conditions. Two commonly used and easy to implement techniques are the Perturb and Observe (P&O) (Ahmed & Salam, 2015; Altwallbah et al., 2022; V. Kumar & Bindal, 2023) and Incremental Conductance (INC) (Belkaid et al., 2016; Bouarroudj et al., 2022; P. Kumar & Shrivastava, 2022).

For a grid-connected PV system, the inverter ensures that the extracted power from the PV panels is properly fed to the grid. This is typically achieved by the regulation of the dc-link voltage to keep it to a constant value which is higher than the grid peak voltage. Conventionally, the dc-link voltage regulation is performed through the use of proportional–integral (PI) controllers, due to their simple operation. However, other techniques including fuzzy logic as well as robust techniques including sliding mode control and their variants have also been proposed (Bisht & Sikander, 2022; Fathi & Parian, 2021; Jendoubi et al., 2020; Kayisli, 2023). PI controllers have to be tuned to obtain optimal proportional and integral gains. Several authors have investigated the application of AI-based techniques for tuning PI controllers. For instance, a fictitious reference iterative tuning (FRIT) method using particle swarm optimisation (PSO) was used to determine optimised parameters for PI controller (Tripathi & Hanamoto, 2015). The resulting FRIT-PSO method demonstrated an improved response in terms of response time and overshoot, compared to the PI parameters generated through the trial and error method. In addition to this, a Fractional Order Proportional – Integral (FO-PI) controller was developed to meet the regulated dc-link voltage at the inverter input. This allowed independent control of the active and reactive power (Lakshmi & Hemamalini, 2018). More recently, a genetic algorithm-based PI controller was presented for regulating the current and dc-link voltage, in order to control the active and reactive powers injected by a PV system to the grid (Farhat et al., 2017). Also, a bandwidth oriented approach was utilised for the determination of PI controller gains, used in a doubly fed induction generator wind turbine system (Zhou & Blaabjerg, 2017). In this work, we are applying the same approach for the PI controller design of a two-stage three-phase grid-connected PV system. Compared to AI-based models, the bandwidth approach for the determination of PI parameters is faster and its computational burden is much lesser. Also, the use of trial-and-error methods does not guarantee optimal values of parameters. In the case of fractional order controller, complex modelling is required.

Harmonic distortion as well as low power factor of non-linear loads are typically considered as the main issues related to power quality (Ahsan et al., 2021). Power electronic inverters, which do not produce pure sinusoidal waveforms, introduce harmonics into the system at the point of common coupling (PCC) with the grid. The aggregation of such harmonics is commonly termed as total harmonic distortion (THD). The IEEE 519 standard stipulates that the maximum permissible THD for low voltage applications is 5% (Comsys, n.d.). The impact of harmonics on the grid has also been thoroughly studied in the past few years (Ahsan et al., 2021; Kazemi-Robati et al., 2022; Lamreoua et al., 2023; Xie et al., 2022). From several sources, it has been established that with an increase in the level of penetration of PV systems, the harmonic distortion level in the grid also increases. In this work, we provide a simple analysis of the THD levels based on the simulated grid-connected system.

This remaining portion of the paper is organised as follows: In [Section 2](#) the system configuration is explained, while [Section 4](#) elaborates on the modelling and control of a grid connected PV system, with the different blocks namely MPPT control, inverter control with the current control loop, as well as the dc-link voltage control loops. In [Section 5](#), two sets of simulations are presented to assess the performance of the PI controllers, using the adopted design methodology, and the results are discussed. Finally, conclusions are drawn in the last section.

## 2. System configuration

Grid-connected PV systems control generally includes two parts, namely maximum power point tracking (MPPT) control and inverter control. [Figure 1](#) shows a block diagram of a grid-connected photovoltaic system with control loops.

### 2.1. MPPT control

The objective of MPPT algorithm is to find the optimal operating point of the PV panel, that is the maximum power point, even in the presence of adverse conditions affecting the irradiance and the temperature of the panel. This is done by controlling the operating point of the PV panel according to the power-voltage characteristics of the PV array. A reference voltage is normally set by the selected MPPT algorithm, while an inner-loop control of the converter is responsible to regulate the system with respect to the reference value. A simple PI controller is typically used to regulate the system, as shown in [Figure 2](#).

### 2.2. Inverter control

The dc-dc converter controls the PV power, while the dc-ac converter (inverter) ensures that the extracted power is properly fed to the grid. This is done by

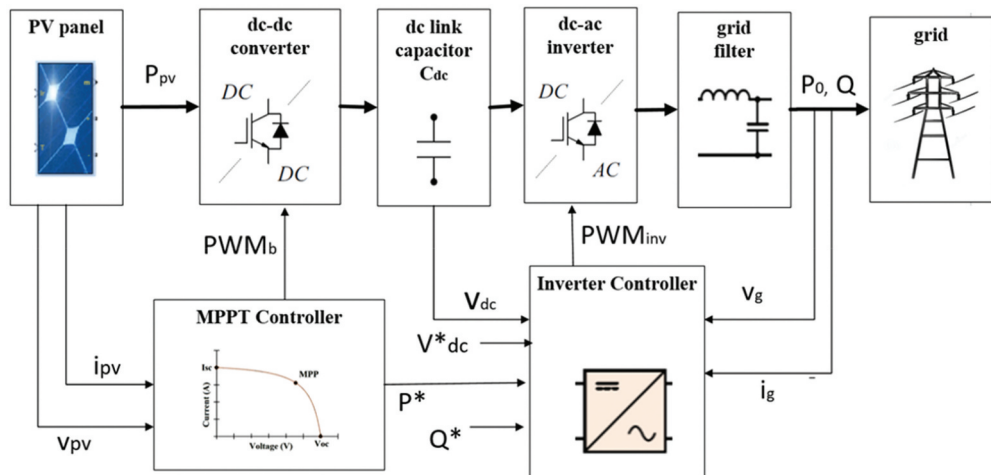


[Figure 1](#). Grid-connected photovoltaic system control.

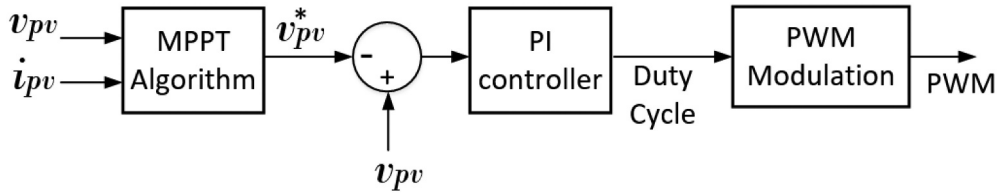


**Figure 2.** PI controller for PV voltage control.

regulating the dc-link voltage, as this voltage must be kept constant for the dc power and ac power to balance. This method is commonly called the voltage control method, whereby the current is controlled indirectly, by measuring and adjusting the dc-link and the supply voltage. This technique is also commonly referred to as ‘indirect current control’ (Dixon & Ooi, 1988). A dual-loop control structure is typically used, whereby the outer control loop is concerned with the voltage or power control, which produces the inner control loop current references. The inner control may be implemented in different reference frames, namely the *abc*, *aβ*, and the *dq* frames.

### 3. System modelling

Figure 3 shows the system modelling of the three-phase, two-level dc-ac converter. An LCL filter is commonly used for such systems, however a single inductor filter can also be used since it has similar characteristics for low frequency (Liserre et al., 2005). The active and reactive power are controlled at the outer loop by a PQ controller or through the dc link voltage regulation (Blaabjerg et al., 2006). The current injected to the grid is controlled by the inner loop, according to a reference set by the outer loop. The inverse Park and Clark transformations, along with the current controller, provides the output reference voltage  $v_{inv}^*$  for the dc-ac controller. This is used for the pulse-width modulation (PWM) which switches the inverter to produce the output voltage  $v_{inv}$ .

#### 3.1. Current control loop modelling

In order to control the output current from the converter, the current controller generates a voltage output reference. Referring to Figure 3, the following equation could be derived:

$$L \frac{di}{dt} + Ri = v_{inv} - v = v_1 - v \quad (1)$$

Where

$L$  : inductance of filter

$R$  : resistance of filter

$v_1$ : output voltage from converter

$v$  : grid voltage

$i$  : grid current

For a 3-phase system, the inverter’s outputs are as follows:

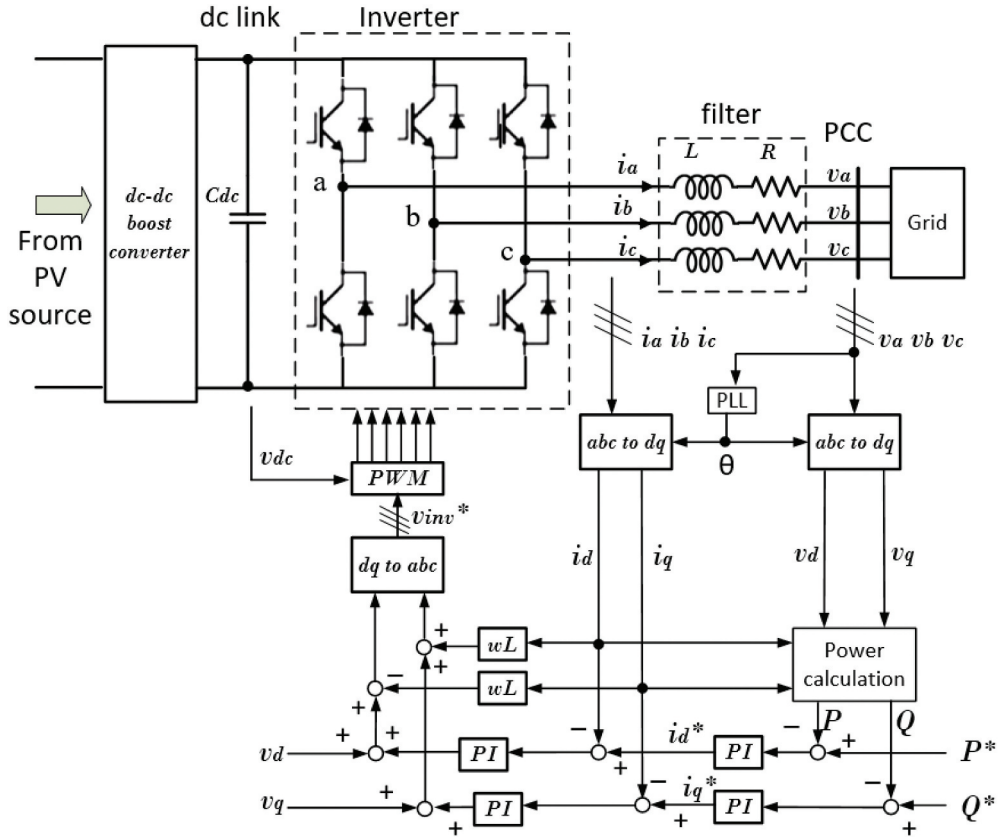


**Figure 3.** System diagram of the 3 phase 2 level dc-ac converter with the dual-loop control structure.

$$L \frac{di_a}{dt} + Ri_a = v_{a1} - v_a \quad (2)$$

$$L \frac{di_b}{dt} + Ri_b = v_{b1} - v_b \quad (3)$$

$$L \frac{di_c}{dt} + Ri_c = v_{c1} - v_c \quad (4)$$

Applying the Clarke and Park frame transformations results in

$$L \frac{di_d}{dt} + Ri_d - \omega Li_q = v_{d1} - v_d \quad (5)$$

$$L \frac{di_q}{dt} + Ri_q + \omega Li_d = v_{q1} - v_q \quad (6)$$

where

$i_d$  and  $i_q$ : currents injected to the grid on the dq reference frame

$v_{d1}$  and  $v_{q1}$ : output voltages from the inverter on the dq axis

$v_d$  and  $v_q$ : load voltages on the dq axis

$\omega$  : frequency of the system

From the Equations (5) and (6), it can be deduced that the output voltage of the inverter can be used to regulate the injected current to the grid. However, there is a coupling between the  $d$  and  $q$  axis output currents, which complicates the system. To work around this issue, a decoupling term as well as a feed-forward voltage is added as follows:

$$v_{d1} + \omega L i_q - v_d = L \frac{di_d}{dt} + R i_d = v_{d1}^* \quad (7)$$

$$v_{q1} - \omega L i_d - v_q = L \frac{di_q}{dt} + R i_q = v_{q1}^* \quad (8)$$

where

$v_{d1}^*$  and  $v_{q1}^*$ : output voltage references

Applying the s-domain transformation

$$v_{d1}^*(s) = L s i_d(s) + R i_d(s) \quad (9)$$

Therefore,

$$v_{d1}^*(s) = i_d(s)(sL + R) \quad (10)$$

$$i_d(s) = \frac{1}{sL + R} v_{d1}^*(s) \quad (11)$$

Also from Equations (7) and (8)

$$v_{d1}^* = v_{d1} + \omega L i_q - v_d \quad (12)$$

Thus

$$v_{d1}^*(s) = v_{d1}(s) + \omega L i_q(s) - v_d(s) \quad (13)$$

Similarly, for the q-axis,

$$i_q(s) = \frac{1}{sL + R} v_{q1}^*(s) \quad (14)$$

and

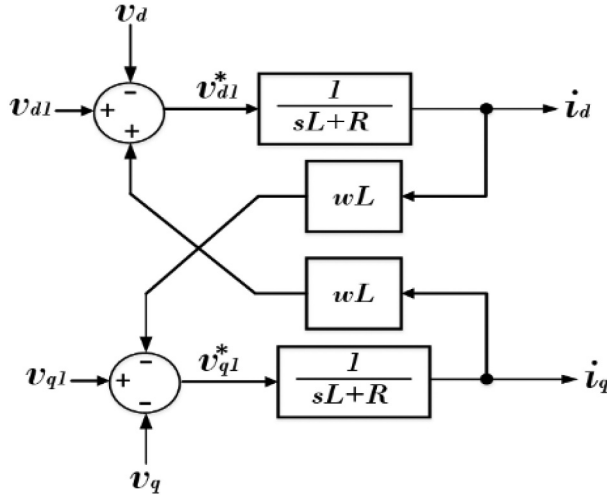
$$v_{q1}^*(s) = v_{q1}(s) - \omega L i_d(s) - v_q(s) \quad (15)$$

Figure 4 shows the block diagram of the ac side control of three-phase dc-ac inverter in the  $dq$ -reference frame, obtained from Equations (7)-(15). The plant transfer functions can be obtained as shown in Equation (16).

$$\frac{i_d(s)}{v_{d1}^*(s)} = \frac{i_q(s)}{v_{q1}^*(s)} = \frac{1}{sL + R} \quad (16)$$

### 3.2. Active and reactive power control loop

The instantaneous active and reactive power in the  $dq$  reference frame can be calculated as:



**Figure 4.** Ac side control of three-phase dc-ac inverters in the dq-reference frame.

$$P = \frac{3}{2} (v_d i_d + v_q i_q) \quad (17)$$

$$Q = \frac{3}{2} (v_q i_d - v_d i_q) \quad (18)$$

By aligning the d-axis to the load/grid voltage,  $v_d = V_m$  (phase voltage amplitude),  $v_q = 0$ . Thus,

$$P = \frac{3}{2} (v_d i_d) = \frac{3}{2} (V_m i_d) \quad (19)$$

$$\frac{P(s)}{i_d(s)} = \frac{3}{2} (V_m) \quad (20)$$

Similarly,

$$Q = -\frac{3}{2} (v_d i_q) = -\frac{3}{2} (V_m i_q) \quad (21)$$

$$\frac{Q(s)}{i_q(s)} = -\frac{3}{2} (V_m) \quad (22)$$

From the Equations (19)-(22), the active and reactive powers are proportional to  $V_m$ , that is the output load voltage amplitude. Hence, it is possible to regulate the active and reactive power, with an open loop, neglecting the inverter losses. However, in practice, a closed loop is employed, as shown in [Figure 3](#), in order to improve the system performance due to load variations and system uncertainties.

### 3.3. DC link control loop

Alternately, by regulating the dc-link voltage across the capacitor, the active power of the dc-ac inverter can be controlled (Teodorescu et al., 2011). This method is typically used in photovoltaic (PV) systems. For a PV system to be able to inject power to the grid, the voltage at the dc-link needs to be higher than that of the grid. The dc-link power and the active power output should be equal, assuming no losses in the inverter. Hence, the power balance equations can be written as shown in Equation (23).

$$\text{dc input power} = \text{output active power}$$

$$v_{dc} C_{dc} \frac{dv_{dc}}{dt} = \frac{3}{2} (v_d i_d + v_q i_q) \quad (23)$$

where

$C_{dc}$ : dc-link capacitance,

$v_{dc}$ : dc-link voltage,

When the d-axis is aligned with the load/grid voltage,  $v_d = V_m$  and  $v_q = 0$ .

Hence, from Equation (23),

$$v_{dc} C_{dc} \frac{dv_{dc}}{dt} = \frac{3}{2} (v_d i_d + v_q i_q) = \frac{3}{2} V_m i_d \quad (24)$$

In the s-domain,

$$v_{dc}(s) C_{dc} V_{dc} s = \frac{3}{2} V_m i_d(s) \quad (25)$$

Hence

$$\frac{v_{dc}(s)}{i_d(s)} = \frac{3}{2} \frac{V_m}{C_{dc} V_{dc} s} \quad (26)$$

where

$V_{dc}$ : average voltage of the dc source

### 3.4. Current controller design

Figure 5 shows the block diagram of the current control loops in  $dq$ -reference frame where

$G_{PI}^d(s)$  : d-component of the PI current controller

$G_{delay}(s)$ : delay due to PWM and computations

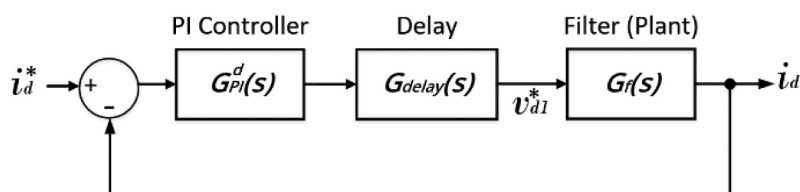


Figure 5. Current control loops in  $dq$ -reference frame.

$G_f(s)$  : filter (plant) transfer function

The  $d$ - and  $q$ -axis components have the same dynamics for the inner loops, so the  $q$ -axis controller is designed in a similar fashion. The transfer functions for the blocks in Figure 5 are given as:

$$G_{PI}^d(s) = k_{pd} + \frac{k_{id}}{s} = \frac{k_{pd}(1 + T_{id}s)}{T_{id}s} \quad (27)$$

$$G_{delay}(s) = \frac{1}{1 + 1.5T_s s} \quad (28)$$

$$G_f(s) = \frac{1}{R + Ls} = \frac{T_f}{L(1 + T_f s)} \quad (29)$$

where

$k_{pd}$  and  $k_{id}$ : proportional and the integral gains of the PI controller

$T_{id} = \frac{k_{pd}}{k_{id}}$  : integrator time constant

$T_s$ : sampling time

$T_f = \frac{L}{R}$  : filter time constant

The cross-coupling ( $\omega Li_q$ ) and the voltage feed-forward ( $v_d$ ) terms are neglected. They are considered as system disturbances. The open-loop transfer function is expressed as

$$G_{ol}^d(s) = G_{PI}^d(s)G_{delay}(s)G_f(s) = \frac{k_{pd}T_f(1 + T_{id}s)}{T_{id}Ls(1 + 1.5T_s s)(1 + T_f s)} \quad (30)$$

Hence, the closed-loop transfer function is obtained from:

$$G_{cl}^d(s) = \frac{G_{ol}^d(s)}{1 + G_{ol}^d(s)} = \frac{k_{pd}T_f(1 + T_{id}s)}{T_{id}Ls(1 + 1.5T_s s)(1 + T_f s) + k_{pd}T_f(1 + T_{id}s)} \quad (31)$$

In order to simplify the closed-loop transfer function,  $T_{id}$  is chosen to have a value equal with that of  $T_f$ .

Hence Equation (31) is simplified as follows:

$$G_{cl}^d(s) = \frac{k_{pd}}{Ls(1 + 1.5T_s s) + k_{pd}} = \frac{\frac{2k_{pd}}{3T_s L}}{s^2 + \frac{2}{3T_s} s + \frac{2k_{pd}}{3T_s L}} \quad (32)$$

This represents a second-order system with

$$\omega_n^2 = \frac{2k_{pd}}{3T_s L} \quad (33)$$

$$2\zeta\omega_n = \frac{2}{3T_s} \quad (34)$$

where

$\omega_n$ : natural frequency

$\zeta$  : damping ratio

The value typically assigned to the damping ratio, resulting in an overshoot of 5% in response to a step input, for an optimally damped system is  $\zeta = \frac{1}{\sqrt{2}}$  (Teodorescu et al., 2011). Thus, the proportional gain  $k_{pd}$  and the integral gain  $k_{id}$  are calculated as:

$$k_{pd} = \frac{L}{3T_s} \quad (35)$$

$$k_{id} = \frac{L}{3T_s T_f} \quad (36)$$

Since

$T_f = \frac{L}{R}$ : filter time constant

$$k_{id} = \frac{L}{3T_s \frac{L}{R}} = \frac{R}{3T_s} \quad (37)$$

The closed-loop transfer function can be approximated as:

$$G_{cl}^d(s) \approx \frac{1}{1 + 3T_s s} = \frac{1}{1 + \tau s} \quad (38)$$

From the above Equation, the bandwidth can be approximated to

$$f_{bw}^d \approx \frac{1}{2\pi\tau} = \frac{1}{6\pi T_s} \quad (39)$$

### 3.5. DC link voltage controller design

The dc-link voltage controller generates the  $d$ -axis current reference,  $i_d^*$ , through an outer loop, as depicted in Figure 6, where  $G_{PI}^v(s)$  is the voltage PI controller, and  $G_v(s)$  represents the plant.

The transfer functions can be represented as follows:

$$G_{PI}^v(s) = k_{pv} + \frac{k_{iv}}{s} = \frac{k_{pv}(1 + T_{iv}s)}{T_{iv}s} \quad (40)$$

$$G_v(s) = \frac{3}{2} \frac{V_m}{C_{dc} V_{dc} s} \quad (41)$$

where

$k_{pv}$  : proportional gain

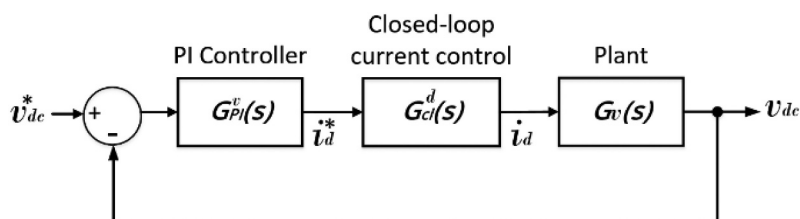


Figure 6. DC-link voltage control loop.

$k_{iv}$  : integral gain

$T_{iv}$  : integrator time constant

From Figure 6, the open-loop transfer function can be expressed as

$$G_{ol}^v(s) = G_{PI}^v(s)G_{cl}^d(s)G_v(s) \quad (42)$$

Using the simplified current control loop of Equation (38),

$$G_{ol}^v(s) \approx \frac{3V_m k_{pv}(1 + T_{iv}s)}{2T_{iv}C_{dc}V_{dc}s^2(1 + 3T_3s)} \quad (43)$$

The phase crossover frequency  $\omega_c$  can be expressed as

$$\omega_c = \frac{1}{\sqrt{3T_s T_{iv}}} \quad (44)$$

Also, the control parameters  $k_{pv}$  and  $k_{iv}$  at the crossover frequency are given by:

$$k_{pv} = \frac{C_{dc}}{2\sqrt{T_s T_{iv}}} \quad (45)$$

$$k_{iv} = \frac{C_{dc}}{2\sqrt{T_s T_{iv}^3}} \quad (46)$$

#### 4. Simulations and results

Two sets of simulations were carried out to assess the performance of the PI controllers, using the design methodology, described in Section 4. In the first instance (Scenario 1), a constant power was fed to the dc link, instead of using the PV panels. For the Scenario 2, the simulation was carried out with PV panels of 55 kW, under varying irradiation levels. The PV panel temperature is kept constant since its effect is negligible compared to that of the irradiance. For both cases, the system parameters are given in Table 1.

**Table 1.** PV array parameters.

Parameter	Value
PV array type	SunPower SPR-305E-WHT-D
Number of series modules	5
Number of parallel strings	36
Array output power at MPP	55 kW
Array output voltage at MPP	305.2 V
Temperature	25°C
dc-dc converter Switching frequency	5 KHz
PV interfacing transformer	165 KVA
Transformer rating	260V/25kV
dc-link capacitor, $C_{dc}$	5 mF
Filter inductance and resistance	2.5 mH and 50 mΩ
dc-link voltage reference	800 V
Grid frequency	50 Hz
Sampling time, $T_s$	50 μs

#### 4.1. Determination of PI parameters for current and voltage loops

Using Equations (35) and (36), as well as the parameters in Table 1, the PI controller parameters for the d-axis current loop are determined as:

$$k_{pd} = 16.7 \text{ and } k_{id} = 333.3$$

The bandwidth can be approximated using Equation (39), which gives

$$f_{bw}^d = 1000 \text{ Hz}$$

For the dc-link voltage controller, the PI parameters can be determined using Equations (45) and (46). The inner (current) loop is typically much faster than the outer (voltage) loop, so as to separate the cascaded control system (Zhou & Blaabjerg, 2017). In fact, the bandwidth of the outer loop is limited between 1/50 and 1/10 of the inner current loop. In this work, we assumed a bandwidth of 100 Hz, therefore considering the outer loop to be 10 times slower than the inner loop. Hence, using Equation (44), the value of  $T_{iv}$  (integrator time constant) can be determined. Substituting this calculated value of  $T_{iv}$  in Equations (45) and (46), the PI parameters were calculated as:

$$k_{pv} = 2.9 \text{ and } k_{iv} = 192.5$$

#### 4.2. Scenario 1 – constant power fed to the DC-link

The model shown in Figure 3 was implemented in Simulink, with constant power fed to the dc-link through a dc power supply of 800 V. The objective was to verify the designed control parameters of the PI controllers, in the given set-up. The simulation results are depicted in Figure 7, whereby the grid voltages, grid currents, dc link voltage and the  $dq$  voltage and current components are shown. It can be observed that after around 0.15 s, the system stabilises. The grid voltage waveforms are almost perfectly sinusoidal. This indicates that the inverter functions as expected. The dc-link voltage is regulated by the action of the PI controllers and remains almost constant after 0.2 s. This indicates that the PI parameters chosen give good results. Also,  $v_q$  as well as  $i_q$  goes to zero, since the d-axis is aligned with the load/grid voltage. The results show that the methodology described in Section 4 holds for a system whereby a constant power was fed to the dc link. The effect of transients is investigated in Scenario 2.

#### 4.3. Scenario 2 – simulation with PV panels under varying irradiation levels

In this scenario, the model of Figure 3 was simulated under varying solar irradiance levels, to validate the performance of the grid connected PV system. The MPPT block was based on the Incremental Conductance Algorithm. The solar irradiation distribution is shown in Figure 8(A) over a specified period of time ranging between 430 and 1000 W/m<sup>2</sup>. The distribution depicts both step as well as ramp increase and decrease in irradiance, thus introducing transients in the system. Basically, the simulation is valid for weather periods, ranging from sunny, with peak irradiance of 1000 W/m<sup>2</sup>, diffused clouds, as well as dark clouds. The temperature, on the other hand, was kept constant at 25°C, since it has a negligible impact on PV performance compared to irradiance. Also, in practice, the

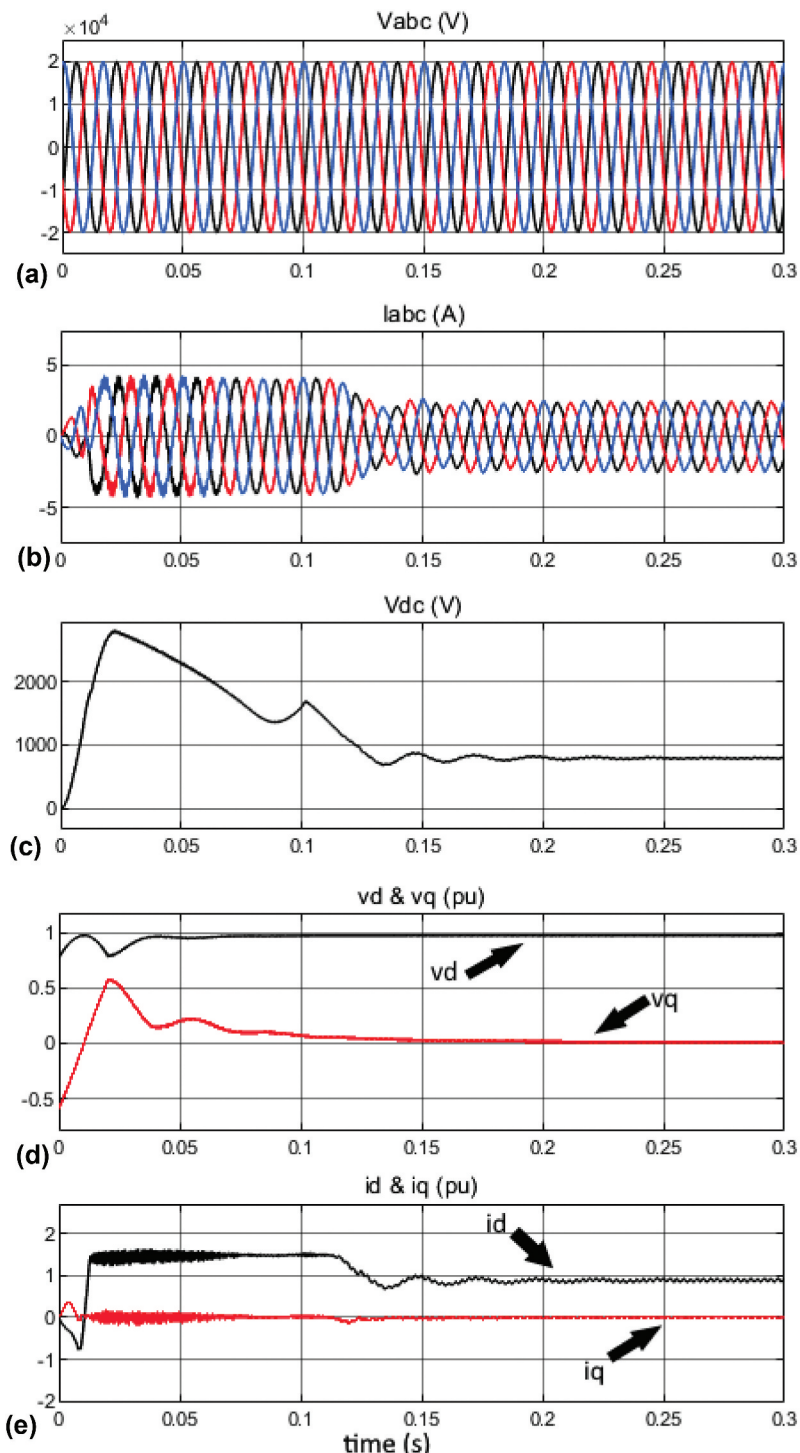


**Figure 7.** Simulation results for the grid-connected three-phase AC/DC converter system : (A) grid line-to-line voltages, (B) grid currents, (C) dc-link voltage, (D) d-axis and q-axis voltage components and (E) d-axis and q-axis current components.

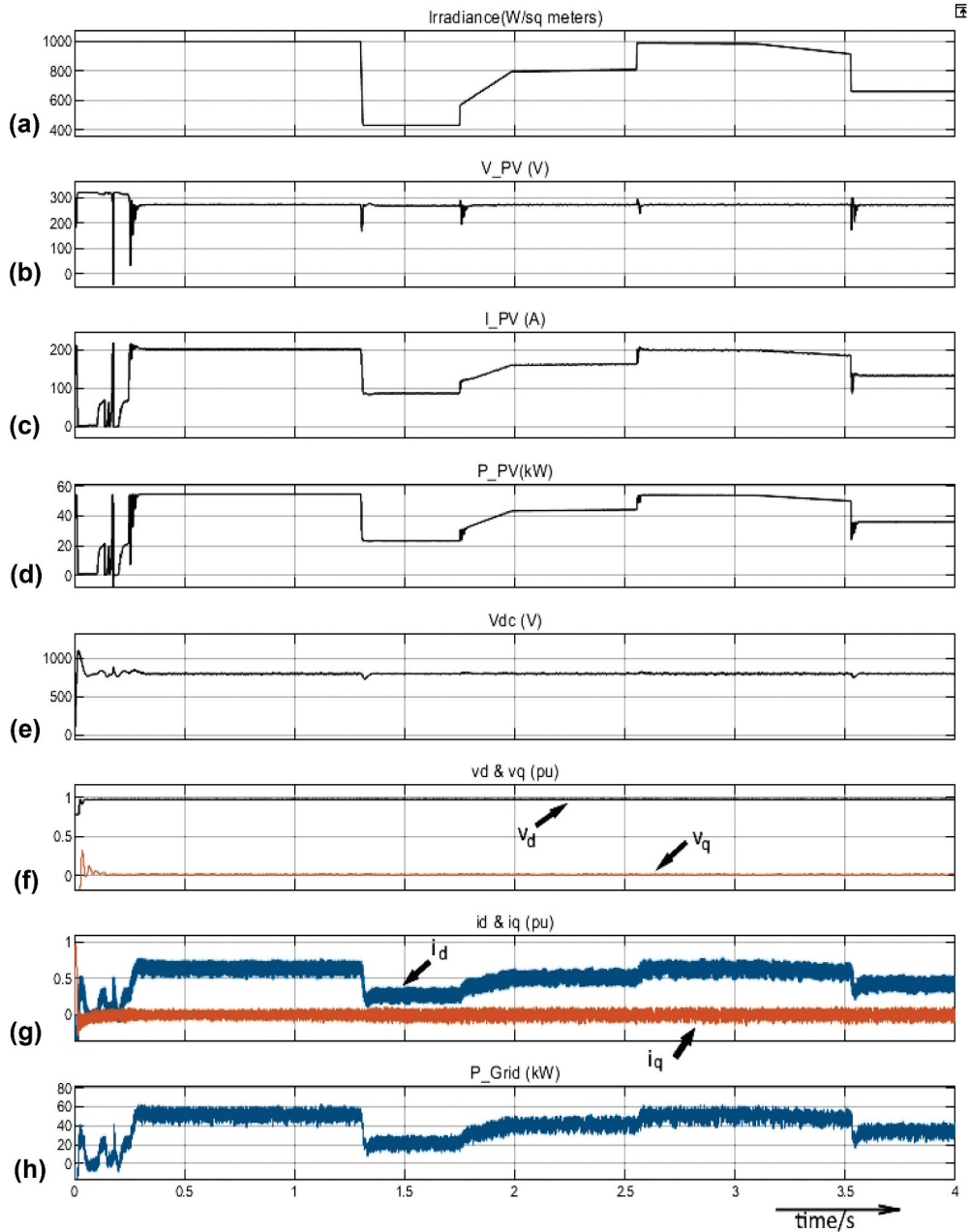


**Figure 8.** Simulation results for the grid-connected three-phase AC/DC converter system : (A) Irradiance, (B) PV voltage, (C) PV current, (D) Mean PV power, (E) dc-link voltage, (F) d-axis and q-axis voltage component, (G) d-axis and q-axis current component and (H) active power injected into the grid.

temperature does not change in a step fashion. Figure 8(B) shows the PV voltage, which is almost constant except for a few transients occurring during drastic changes in irradiance. Figure 8(C) depicts the variation of the output current from the PV array, before the dc-dc boost converter. It can be observed that the PV array current closely follows the irradiance

distribution. The current is maximum at 200 A, for an irradiance of  $1000 \text{ W/m}^2$ , and diminishes as the radiation falls. Also, at  $t = 3.52 \text{ s}$ , there is a drastic fall in irradiance from 915 to around  $660 \text{ W/m}^2$ . The current experiences a transient fall and stabilises back to 130 A in less than 0.1 s. The PV output power is shown in Figure 8(D). The variation closely follows the distribution of the irradiance. Also, the maximum output power observed from the plot is at 55 kW, which tallies with the PV panel specifications. It can also be concluded that the Incremental Conductance MPPT algorithm is very efficient in tracking the maximum power, even in the presence of large variations in the irradiance. Figure 8(E) shows the dc-link voltage. The reference dc link voltage was set to 800 V. From this figure, it can be concluded that the dc voltage tracks the reference dc voltage. Figure 8(F) depicts the variation of the  $d$  and  $q$  axis voltages. As expected, the  $q$  components go to zero, while the per unit (pu) value of  $d$ -axis voltage component,  $v_d = 1$ . Figure 8(G) depicts the variation of the  $d$  and  $q$  axis currents. The variation of the direct axis current,  $i_d$  follows the irradiance distribution, while  $i_q$  is set to zero. Figure 8(H) shows the variation of the active power injected to the grid. It tallies with the input power from the PV panels.

Figure 9 shows the three-phase line voltage waveforms at the grid interface. It can be observed that the inverter produces a balanced waveform that is fed to the grid.

#### 4.4. Effect of parameter mismatch on controller performance

In this section, the effect of parameter mismatch between the controller and the transmission-line filter is investigated. As shown in Equations (35), the filter inductance  $L$  is an important factor in the calculation of the gains for the current loop. The initial value set for the filter inductance  $L$  was  $2.5\text{mH}$ . Assuming this value to be  $L_f$ , the filter inductance is varied from  $0.5L_f$  to  $2L_f$ , and the effect on the dc-link voltage as well as the active power injected into the grid is investigated. As shown in Figure 10,  $V_{dc}$  stabilises around  $0.17 \text{ s}$ , and settles to its reference value, for all  $L$  between  $0.5L_f$  and  $2L_f$ . This shows that the PI controller is indeed robust. In

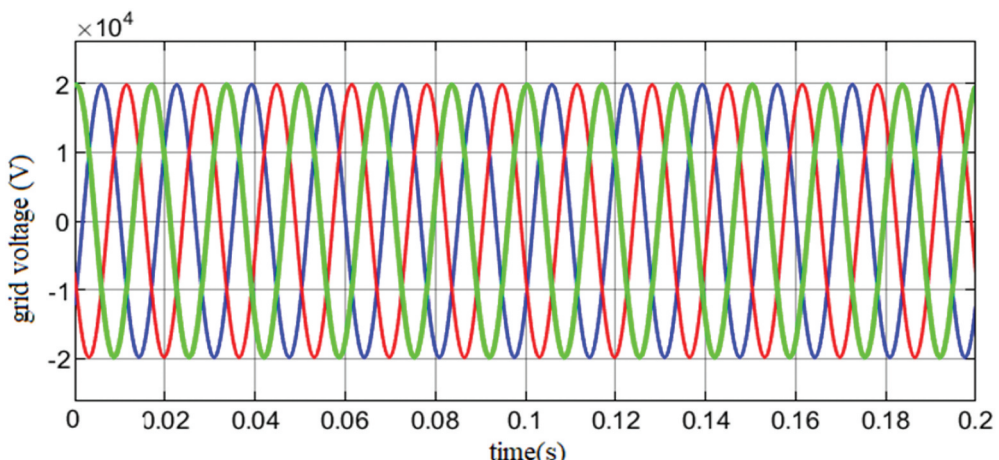
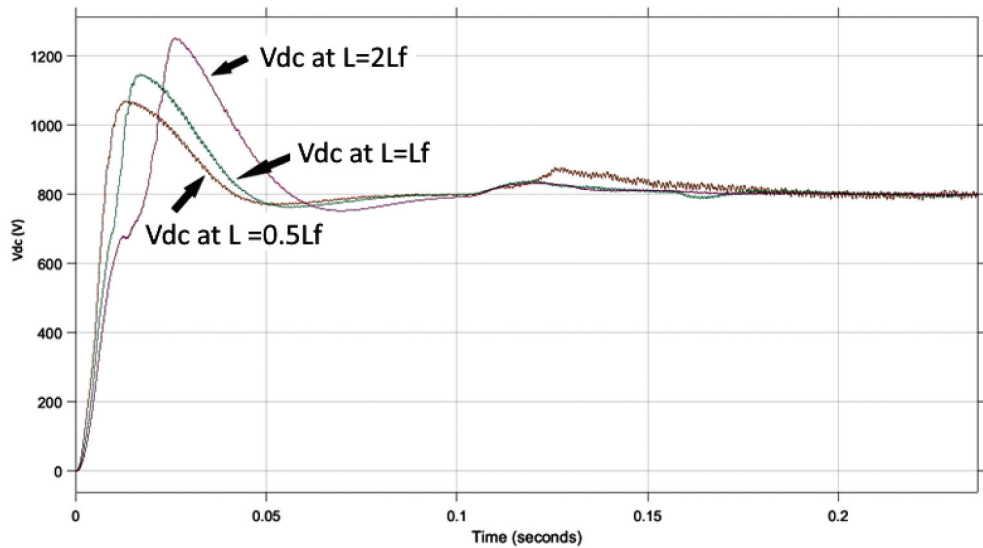
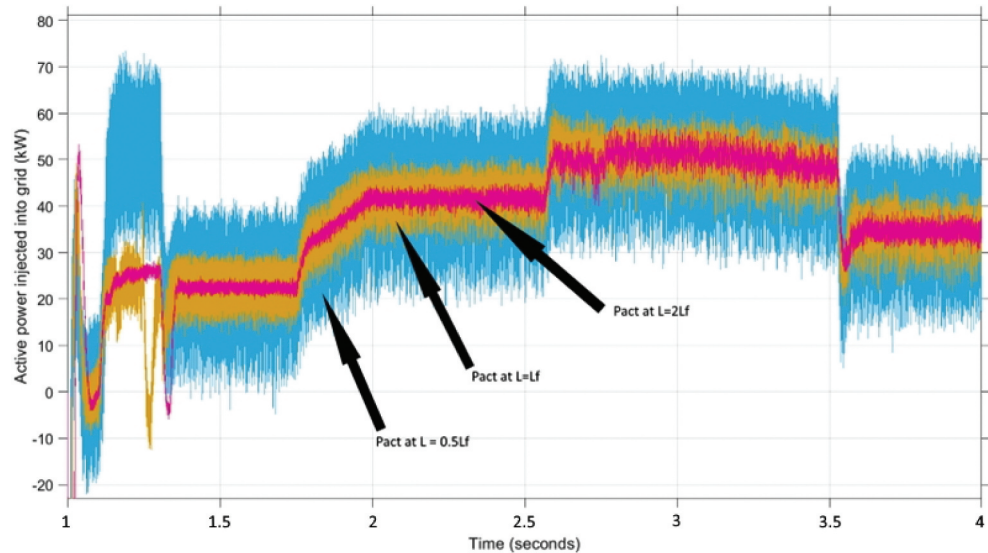


Figure 9. Three-phase grid voltage.



**Figure 10.** Dc voltage for different values of  $L$ .



**Figure 11.** Active power injected into the grid for different values of  $L$ .

**Figure 11**, the variation of the active power injected into the grid for different values of  $L$  is depicted. As the value of  $L$  increases, the ripples diminish. However, the mean value of the active power ( $P_{act}$ ) remains almost constant with the variation in  $L$  between  $0.5 L_f$  and  $2 L_f$ .

**Table 2.** THD analysis with different  $L_f$  values.

$L_f/\text{mH}$	%THD <sub>i</sub>	%THD <sub>v</sub>
2.5	10.5	0.13
5.0	6.06	0.05
7.5	4.20	0.02

#### 4.5. Total Harmonic Distortion (THD) of the injected current and voltage

The THD analysis of the injected current and voltage is performed in this section. The filter inductance is varied, and the corresponding current THD (THD<sub>i</sub>) as well as the voltage THD (THD<sub>v</sub>) is observed. From Figure 11, it can be deduced that a higher value of L causes lesser ripples. Similarly, the THD<sub>i</sub> and THD<sub>v</sub> levels decrease with an increase in L, as shown in Table 2.

Figure 12 shows the current waveforms as well as the percentage THD<sub>i</sub> values for  $L_f = 2.5\text{mH}$  and  $L_f = 7.5\text{mH}$ . The percentage of THD<sub>v</sub> variation is very low compared to that of THD<sub>i</sub>.

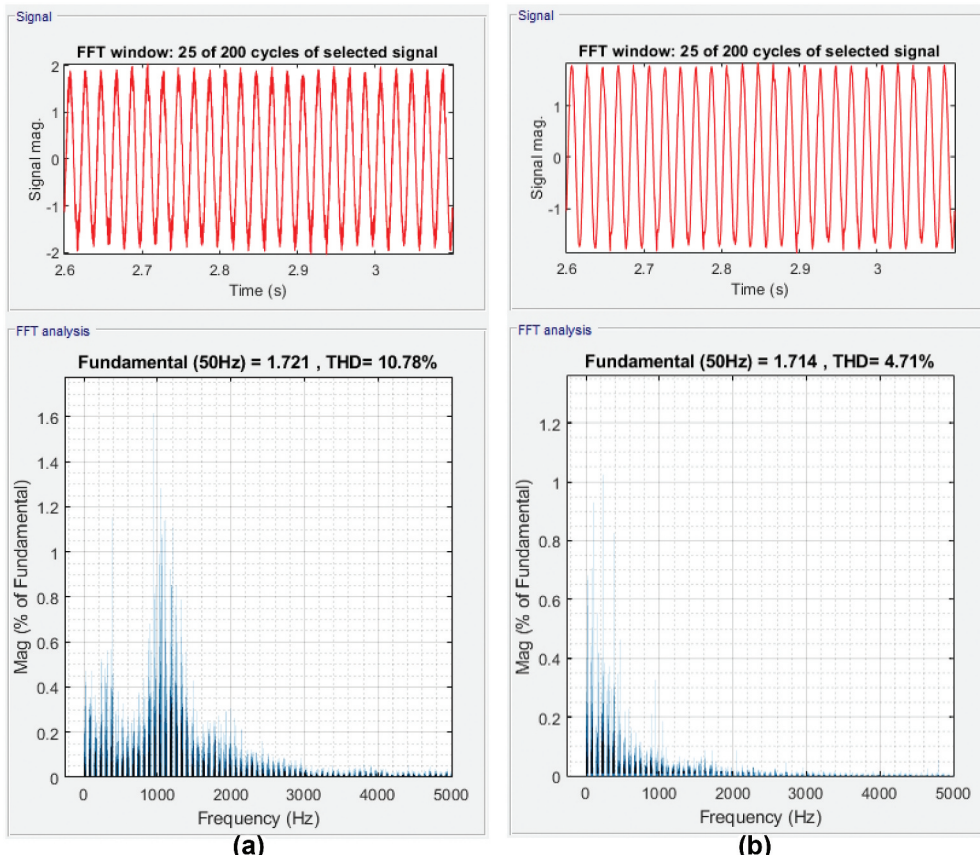


**Figure 12.** Percentage THDi for different values of L: (A)  $L=2.5\text{mH}$ , (B)  $L=7.5\text{ mH}$ .

Several techniques have been discussed in the literature to improve the output of signals with respect to THD. For example, three-level neutral-point-clamped (NPC) inverters having low filter losses have been proposed (Beniwal et al., 2021). Recently multilevel inverters for grid connected PV systems have been the subject of high interest, for THD minimisation (Barbie et al., 2023; Venkedesh et al., 2022).

## 5. Conclusion and further work

This paper focuses on the bandwidth-oriented approach for the determination of PI parameters, for the voltage and current loops, for a three-phase two-stage grid-connected PV system. The mathematical modelling of this configuration, with its inner current loop and the outer voltage loops was discussed. The system involved a PV array, dc-dc converter, Incremental Conductance MPPT algorithm, dc-ac inverter, grid filter and the grid. The MPPT and the inverter controls were also implemented. The entire system was simulated using Matlab Simulink. The PV array was subjected to an irradiance distribution with both step and ramp changes, to simulate extreme conditions with transients. Two sets of simulations were run to validate the model. The results were conclusive and showed that in the presence of varying irradiance, the controls of MPPT and voltage source inverter performed very satisfactorily, to keep the dc voltage at the dc link almost constant. The robustness of the PI controller was also demonstrated. Compared to AI-based models, the bandwidth approach for the determination of PI parameters is faster and its computational burden is much lesser. Also, the use of trial-and-error methods does not guarantee optimal values of parameters. In the case of fractional order controller, complex modelling is required. Besides, in industry, PI controllers with fast and straightforward tuning methods are preferred. The bandwidth approach could further be applied to hybrid systems with multiple sources of renewables. As further work, this approach could be enhanced by the use of machine learning techniques, for a better estimation of PI parameters. Further, the application of multilevel inverters for grid connected PV systems could be investigated for THD minimisation.

## Abbreviations

FO-PI	fractional order proportional – integral
FRIT	fictitious reference iterative tuning
INC	incremental conductance
MPPT	maximum power point tracking
PCC	point of common coupling
PCU	power conditioning unit
PI	proportional–integral
P&O	perturb and observe
PSO	particle swarm optimisation
PV	photovoltaic
PWM	pulse-width modulation

## Disclosure statement

No potential conflict of interest was reported by the authors.

## ORCID

Anshu Prakash Murdan  <http://orcid.org/0000-0003-1073-721X>

## References

- Abdulhasan Salim, J., Albaker, B. M., Shyaa Alwan, M., & Hasanuzzaman, M. (2022). Hybrid MPPT approach using cuckoo search and grey wolf optimizer for PV systems under variant operating conditions. *Global Energy Interconnection*, 5(6), 627–644. <https://doi.org/10.1016/J.GLOEI.2022.12.005>
- Ahmed, J., & Salam, Z. (2015). An improved perturb and observe (P&O) maximum power point tracking (MPPT) algorithm for higher efficiency. *Applied Energy*, 150, 97–108. <https://doi.org/10.1016/j.apenergy.2015.04.006>
- Ahsan, S. M., Khan, H. A., Hussain, A., Tariq, S., & Zaffar, N. A. (2021). Harmonic analysis of grid-connected solar pv systems with nonlinear household loads in low-voltage distribution networks. *Sustainability*, 13(7), 3709. <https://doi.org/10.3390/su13073709>
- Altwallbah, N. M. M., Radzi, M. A. M., Azis, N., Shafie, S., & Zainuri, M. A. A. M. (2022). New perturb and observe algorithm based on trapezoidal rule: Uniform and partial shading conditions. *Energy Conversion and Management*, 264, 115738. <https://doi.org/10.1016/J.ENCONMAN.2022.115738>
- Barbie, E., Kuperman, A., & Baimel, D. (2023). Current-THD minimization in multilevel inverters with variable DC ratios utilizing a generic closed-form analytic formulation of line-voltage WTHD. *Alexandria Engineering Journal*, 66, 211–239. <https://doi.org/10.1016/J.AEJ.2022.11.039>
- Belkaid, A., Colak, I., & Isik, O. (2016). Photovoltaic maximum power point tracking under fast varying of solar radiation. *Applied Energy*, 179, 523–530. <https://doi.org/10.1016/j.apenergy.2016.07.034>
- Beniwal, N., Tafti, H. D., Farivar, G. G., Ceballos, S., Pou, J., & Blaabjerg, F. (2021). A control strategy for dual-input neutral-point-clamped inverter-based grid-connected photovoltaic system. *IEEE Transactions on Power Electronics*, 36(9), 9743–9757. <https://doi.org/10.1109/TPEL.2021.3063745>
- Bisht, R., & Sikander, A. (2022). An improved method based on fuzzy logic with beta parameter for PV MPPT system. *Optik*, 259, 168939. <https://doi.org/10.1016/J.IJLEO.2022.168939>
- Blaabjerg, F., Teodorescu, R., Liserre, M., & Timbus, A. V. (2006). Overview of control and grid synchronization for distributed power generation systems. *IEEE Transactions on Industrial Electronics*, 53(5), 1398–1409. <https://doi.org/10.1109/TIE.2006.881997>
- Bollipo, R. B., Mikkili, S., & Bonthagorla, P. K. (2021). Hybrid, optimal, intelligent and classical PV MPPT techniques: A review. *CSEE Journal of Power and Energy Systems*, 7(1), 9–33. <https://doi.org/10.17775/CSEJPES.2019.02720>
- Bouarroudj, N., Benlahbib, B., Sedraoui, M., Feliu-Batlle, V., Bechouat, M., Boukhetala, D., & Boudjemaa, F. (2022). A new tuning rule for stabilized integrator controller to enhance the indirect control of incremental conductance MPPT algorithm: Simulation and practical implementation. *Optik*, 268, 169728. <https://doi.org/10.1016/J.IJLEO.2022.169728>
- Debnath, D., & Chatterjee, K. (2015). Two-stage solar Photovoltaic-based stand-alone scheme having battery as energy storage element for rural deployment. *IEEE Transactions on Industrial Electronics*, 62(7), 4148–4157. <https://doi.org/10.1109/TIE.2014.2379584>
- Dixon, J., & Ooi, B. T. (1988). Indirect current control of a unity power factor sinusoidal current boost type three-phase rectifier. *IEEE Transactions on Industrial Electronics*, 35(4), 508–515. <https://doi.org/10.1109/41.9172>
- Farhat, M., Hussein, M., & Atallah, A. M. (2017). Bandwidth oriented proportional-integral controller design for back-to-back power converters in DFIG wind turbine system. *2017 Nineteenth International Middle East Power Systems Conference (MEPCON)*, 145–151. <https://doi.org/10.1109/MEPCON.2017.8301177>
- Fathi, M., & Parian, J. A. (2021). Intelligent MPPT for photovoltaic panels using a novel fuzzy logic and artificial neural networks based on evolutionary algorithms. *Energy Reports*, 7, 1338–1348. <https://doi.org/10.1016/J.EGXR.2021.02.051>

- Hassan, A., Bass, O., & Masoum, M. A. S. (2023). An improved genetic algorithm based fractional open circuit voltage MPPT for solar PV systems. *Energy Reports*, 9, 1535–1548. <https://doi.org/10.1016/J.EGYR.2022.12.088>
- IRENA. (2019). *Renewable capacity highlights*. March, 1–2. [www.irena.org/publications](http://www.irena.org/publications).
- Jendoubi, A., Tlili, F., & Bacha, F. (2020). Sliding mode control for a grid connected PV-system using interpolation polynomial MPPT approach. *Mathematics and Computers in Simulation*, 167, 202–218. <https://doi.org/10.1016/J.MATCOM.2019.09.007>
- Kanaan, H. Y., Caron, M., & Al-Haddad, K. (2014). Design and implementation of a two-stage grid-connected high efficiency power load emulator. *IEEE Transactions on Power Electronics*, 29 (8), 3997–4006. <https://doi.org/10.1109/TPEL.2013.2295023>
- Kayisli, K. (2023). Super twisting sliding mode-type 2 fuzzy MPPT control of solar PV system with parameter optimization under variable irradiance conditions. *Ain Shams Engineering Journal*, 14 (1), 101950. <https://doi.org/10.1016/J.ASEJ.2022.101950>
- Kazemi-Robati, E., Sepasian, M. S., Hafezi, H., & Arasteh, H. (2022). PV-hosting-capacity enhancement and power-quality improvement through multiobjective reconfiguration of harmonic-polluted distribution systems. *International Journal of Electrical Power & Energy Systems*, 140, 107972. <https://doi.org/10.1016/J.IJEPE.2022.107972>
- Kumar, V., & Bindal, R. K. (2023). MPPT technique used with perturb and observe to enhance the efficiency of a photovoltaic system. *Materials Today: Proceedings*. <https://doi.org/10.1016/J.MATPR.2023.01.002>
- Kumar, P., & Srivastava, A. (2022). Maximum power tracking from solar PV system by using fuzzy-logic and incremental conductance techniques. *Materials Today: Proceedings*. <https://doi.org/10.1016/J.MATPR.2022.11.117>
- Lakshmi, M., & Hemamalini, S. (2018). Decoupled control of grid connected photovoltaic system using fractional order controller. *Ain Shams Engineering Journal*, 9(4), 927–937. <https://doi.org/10.1016/J.ASEJ.2016.06.002>
- Lamreoua, A., Benslimane, A., Boucnaif, J., Hairech, K., Adaliou, A., & Elouariachi, M. (2023). Current harmonic reduction for grid-connected photovoltaic system (PV) based on improved control of three-phase seven-level PUC inverter. *Materials Today: Proceedings*, 72, 3536–3543. <https://doi.org/10.1016/J.MATPR.2022.08.266>
- Liserre, M., Blaabjerg, F., & Hansen, S. (2005). Design and control of an LCL-filter-based three-phase active rectifier. *IEEE Transactions on Industry Applications*, 41(5), 1281–1291. <https://doi.org/10.1109/TIA.2005.853373>
- Manna, S., Singh, D. K., Akella, A. K., Kotb, H., AboRas, K. M., Zawbaa, H. M., & Kamel, S. (2023). Design and implementation of a new adaptive MPPT controller for solar PV systems. *Energy Reports*, 9, 1818–1829. <https://doi.org/10.1016/J.EGYR.2022.12.152>
- Oshaba, A. S., Ali, E. S., & Abd Elazim, S. M. (2017a). PI controller design for MPPT of photovoltaic system supplying SRM via BAT search algorithm. *Neural Computing & Applications*, 28(4), 651–667. <https://doi.org/10.1007/s00521-015-2091-9>
- Oshaba, A. S., Ali, E. S., & Abd Elazim, S. M. (2017b). PI controller design using ABC algorithm for MPPT of PV system supplying DC motor pump load. *Neural Computing & Applications*, 28(2), 353–364. <https://doi.org/10.1007/s00521-015-2067-9>
- Power quality – IEEE 519-2022 - Comsys. (n.d.). Retrieved January 27, 2023, from <https://comsys.se/our-adf-technology/power-quality-ieee-519-2022/>
- Teodorescu, R., Liserre, M., & Rodriguez, P. (2011). *Grid converters for photovoltaic and wind power systems* (Vol. 29). John Wiley & Sons.
- Tripathi, R. N., & Hanamoto, T. (2015). FRIT based optimized PI tuning for DC link voltage control of grid connected solar PV system. *IECON 2015 - 41st Annual Conference of the IEEE Industrial Electronics Society*, 1567–1572. <https://doi.org/10.1109/IECON.2015.7392324>
- Venkadesh, R., AnandhaKumar, R., & Renukadevi, G. (2022). THD reduction in measurement of H - Bridge multilevel inverter using pulse modulated switching integrated with linear quadratic Regulator. *Measurement: Sensors*, 24, 100435. <https://doi.org/10.1016/J.MEASEN.2022.100435>

- Xiao, W., Edwin, F. F., Spagnuolo, G., & Jatskevich, J. (2013). Efficient approaches for modeling and simulating photovoltaic power systems. *IEEE Journal of Photovoltaics*, 3(1), 500–508. <https://doi.org/10.1109/JPHOTOV.2012.2226435>
- Xie, X., Peng, F., & Zhang, Y. (2022). A data-driven probabilistic harmonic power flow approach in power distribution systems with PV generations. *Applied Energy*, 321, 119331. <https://doi.org/10.1016/J.APENERGY.2022.119331>
- Zhou, D., & Blaabjerg, F. (2017). Bandwidth oriented proportional-integral controller design for back-to-back power converters in DFIG wind turbine system. *IET Renewable Power Generation*, 11 (7), 941–951. <https://doi.org/10.1049/iet-rpg.2016.0760>